

Insights on the Interfacial Processes Involved in the Mechanical and Redox Stability of the $\text{BaCe}_{0.65}\text{Zr}_{0.20}\text{Y}_{0.15}\text{O}_{3-\delta}-\text{Ce}_{0.85}\text{Gd}_{0.15}\text{O}_{2-\delta}$ Composite

Cecilia Mortalò, Marta Boaro,* Elena Rebollo, Valentina Zin, Eleonora Aneggi, Monica Fabrizio, and Alessandro Trovarelli



Cite This: *ACS Appl. Energy Mater.* 2020, 3, 9877–9888



Read Online

ACCESS |



Metrics & More



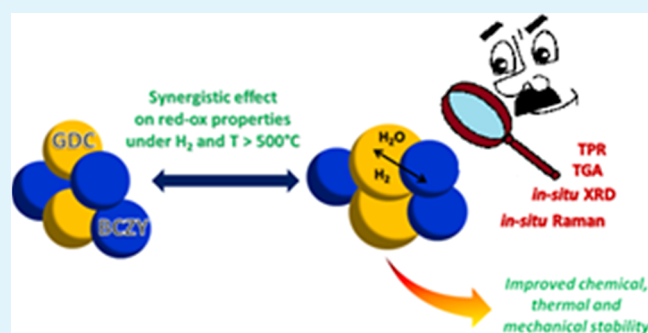
Article Recommendations



Supporting Information

ABSTRACT: Ceramic fuel cells and H_2 permeation membranes are key technologies to accelerate the transition from a carbon economy based on fossil fuels to a H_2 economy based on the use of renewable resources. The competitiveness of these technologies in the market depends on the identification and optimization of stable and effective low-cost materials. Perovskite–fluorite ceria-based composites show suitable properties, and studies on the mechanism that rules their mechanical, thermal, and redox stability are crucial for further technological advances. This study focuses on the redox behavior of $\text{BaCe}_{0.65}\text{Zr}_{0.20}\text{Y}_{0.15}\text{O}_{3-\delta}-\text{Ce}_{0.85}\text{Gd}_{0.15}\text{O}_{2-\delta}$ (BCZY–GDC) dual-phase ceramic. Temperature-programmed reduction, thermogravimetry, temperature-dependent X-ray diffraction, and Raman analyses are used to understand the dynamics of the interaction between the ceramic oxide components. It is shown how the simultaneous occurrence of structural changes in BCZY and GDC reduction helps in decreasing the mechanical stresses induced by temperature and by the reducing atmosphere. The interfacial processes between the single GDC and BCZY oxides contribute to limit reduction of GDC in the composite, which allows complete reversibility of the redox process investigated in this study. Thus, it is suggested that the redox behavior of this class of materials may be a descriptor of their mechanical and thermal stability.

KEYWORDS: Dual-phase ceramic composites, temperature-programmed analyses, redox behavior, proton conductors, ceria-based oxides



1. INTRODUCTION

Nowadays, social, economic, and environmental issues related to the use of fossil fuels boost the rapid transition to a sustainable and cleaner energy system based on renewable resources. With this prospect, hydrogen as an energy vector has been considered a fundamental key enabling technology.^{1,2} A strategy for accelerating this transition could be the optimization and strengthening of hydrogen-related technologies that make use of fossil fuel as feedstock. Examples of this approach are the use of membranes for hydrogen purification in the conventional hydrocarbon-reforming processes and the spreading of intermediate temperature-solid oxide fuel cell (IT-SOFC) technology among the highly efficient electrochemical approaches to produce electric power.³ The progress of protonic and mixed protonic–electronic conductors^{4–15} as well as the development of new materials with multifunctional conduction properties is crucial for the advancement of both membranes and IT-SOFC technologies.^{16–21} An approach to tune the conductivity of materials according to their area of application is the preparation of two-phase composites containing oxides with different types of conductivity. The

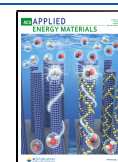
combination of perovskite and fluorite phases based on cerium oxide is often explored to tune proton and oxygen ion conductivity of IT-SOFC electrolytes^{16,17} and the mixed ion electronic conductivity of hydrogen-selective ceramic membranes.^{10,18} This may offer many advantages; for example, by integrating two proton and oxygen conductive phases, it is possible to enhance material conductivity and the power-out of ceramic fuel cells at lower temperatures.²²

Low operative temperature potentially lowers the cost of these systems due to reduced stack and balance-of-plant constraints, while it improves their reliability and stability in thermal cycles. In addition, fast transport of protons at low temperatures favors kinetics and thermodynamics for higher

Received: July 6, 2020

Accepted: September 8, 2020

Published: September 8, 2020



value chemical production through processes such as hydrogenation/dehydrogenation.⁹

On the other hand, the use of protonic–electronic conductors for H₂ selective membranes as an alternative to Pd-based materials offers the advantage of a cost-effective separation process with improved chemical and mechanical robustness. Moreover, protonic–electronic membranes can operate at higher temperatures, which favors an easier integration with cascade industrial processes that require pressurized and hot hydrogen.^{10,11}

In the context of this latter application, we have recently developed a mixed proton–electron conductor based on BaCe_{0.65}Zr_{0.20}Y_{0.15}O_{3-δ} (BCZY) and Ce_{0.85}Gd_{0.15}O_{2-δ} (GDC), which resulted to be one of the most effective membranes for H₂ separation at 750 °C with good robustness toward CO₂-containing atmosphere^{19,20} and acceptable tolerance to H₂S impurity.²¹ The optimization of this material stems from previous studies on individual components. The use of neutron and high-resolution diffraction techniques and Raman spectroscopic studies have provided an understanding of the correlations among structure, composition, and conductivity for both the cerate–zirconate^{23–29} and gadolinium-doped cerium oxide.^{30,31} These studies have contributed to rationalize the behavior of the BCZY–GDC composite under operating conditions. The proton conduction and H₂ transport in BCZY occur through the Grotthuss mechanism. This mechanism involves a specific reorientation of the hydroxides and the transfer of protons by hopping between adjacent oxygen ions.^{32,33} It implies an ambipolar diffusion of protons and electrons and also of hydroxyl groups (in the presence of oxygen vacancies and water). The reduction of gadolinium-doped cerium oxide, which generally starts in the range of 500–600 °C,^{34,35} promotes the enhancement of the electronic conductivity and concentration of oxygen vacancies in the dual-phase material, thus boosting proton conductivity and hydrogen transport above 600 °C. On the other hand, such a composite showed potential mechanical fragility when exposed to hydrogen flow at high temperatures. In fact, proton incorporation and reduction of Ce⁴⁺ to the larger Ce³⁺ cation cause expansion of BCZY and GDC lattices,^{36,37} respectively, with consequent mechanical strains that could affect the performance and lifespans of devices based on this material.

Recently, we have demonstrated the importance of fundamental studies on the composite to ascertain its stability under operating conditions.³⁸ The study showed that under reducing and humidified environment, BCZY and GDC behave synergistically with their expansion coefficients converging toward a common value, thus favoring the mechanical stability of BCZY–GDC-based systems.

In this study, we gained insights into the mechanism that contributes to mitigating the effect of lattice expansion of the two oxides in the composite. Thermogravimetric analysis (TGA), temperature-programmed reduction (TPR), X-ray diffraction (XRD), and Raman spectroscopy were used to investigate the BCZY–GDC synergistic behavior during a redox cycle. In spite of the fact that the functionality of this composite strongly depends on its reduction–oxidation behavior, to the best of our knowledge, this is the first study that focuses on its redox properties. We found that an interfacial process can explain the mechanical and redox stability of the composite under reducing conditions, suggesting that the redox behavior of perovskite–fluorite

materials could be used as a good descriptor of their mechanical and thermal stability.

2. EXPERIMENTAL SECTION

2.1. Preparation of Materials. BCZY powder was purchased from Marion Technologies (France), while GDC powder was prepared by solid-state synthesis.¹⁹ In order to obtain the composite BCZY–GDC, the two powders were ball milled in proportion 46 wt % (BCZY) and 54 wt % (GDC) following a previously reported procedure.¹⁹ Milling was carried out on powders suspended in ethanol for 1 h with zirconia balls (Pulverisette 6, Fritsch). Afterward, the mixture was dried, ground in a mortar, and sieved in range 45–150 meshes.

In order to study materials with properties similar to those encountered in membrane and electrolyte applications, the powders were pelletized and sintered under air at high temperature (1450 °C) and then ground and sieved through 45 and 150 meshes. Physicochemical properties of the powders are reported in a previous study.¹⁹

2.2. Characterization Techniques. **2.2.1. XRD Analyses.** XRD analyses were performed by using a Philips X'Pert diffractometer operating at 40 kV and 40 mA using nickel-filtered Cu K(α) radiation. Phase identification was done from the diffractograms recorded with a step size of 0.02° and a counting time of 40 s per angular abscissa in the range of 20–145 2θ degrees. Rietveld refinement of the XRD pattern was performed by means of GSAS–EXPGUI program.^{39,40} Diffractograms were also collected using a hot chamber (Anton Paar) after reduction and oxidation ramps. The reducing gas was a mixture of 4.58% H₂ in N₂, while air flow was used for the oxidative ramp. Dry gases were fed through stainless steel lines from tanks. In both reducing and oxidizing ramps, each sample was heated at 10 °C/min from room temperature (RT) to 750 °C and diffractograms were collected after 30' isotherm at the set point temperature (50, 200, 350, 550, and 750 °C). To avoid structural changes during XRD acquisition, the counting time was shortened to 15 s and the 2θ degrees range was set from 20 to 100. The experiments were conducted following this procedure: (i) reduction ramp from RT to 750 °C, (ii) isothermal step at 750 °C for 120', (iii) cooling to 50 °C, (iv) purging in N₂ 15', (v) oxidation at 500 °C for 1 h, and then (vi) oxidation ramp to 750 °C.

2.2.2. Raman Analyses. Raman spectra were collected with an XploRA Plus confocal micro-Raman system (Horiba, Japan) on sample powders deposited on a thin glass used in microscopy for optical observations. BCZY and GDC materials showed different adsorption of Raman source; therefore, the conditions used for the comparison were optimized to obtain an acceptable response for both materials. The Raman spectra were collected in the range 50–1200 cm⁻¹ using a 532 nm Nd:YAG laser at the power of 7.1 mW with a grating filter of 2400 cm⁻¹. The accumulation time was 18–20 s with two scans. The comparison of the results has been made among normalized spectra corrected for their baseline. The results were analyzed by fitting the Raman spectra with the proprietary software LabSpec6. The in situ experiments were carried out in a Linkam CR100 chamber by using 20–30 mg of samples. Before the redox cycle, all specimens were pretreated in the air at 600 °C to clean the surface. This procedure also allowed powders to settle in the sample holder, ensuring a good reproducibility of the results. The redox cycle consisted of an oxidizing ramp (10 °C/min) up to 740 °C in air flow (30 cm³/min) as reference followed by a reducing ramp in 4.58% H₂ in N₂ flow (30 cm³/min) up to 800 °C. Spectra were recorded every 20 or 40 °C with a stabilization time of 20 s. After reduction, the samples were re-oxidized at 600 °C (Figure S1). The final effect of the redox cycle was checked at RT by recording spectra in at least four points of the sample.

2.2.3. TPR Analyses. TPR experiments were carried out in a Micromeritics Autochem II 2920 analyzer under a 4.58% H₂/N₂ flow passing through the sample (35 STP cm³/min) with a ramp of 10 °C/min from RT up to 940 °C. The samples were previously oxidized at 500 °C for 1 h to eliminate adsorbates such as carbonates and

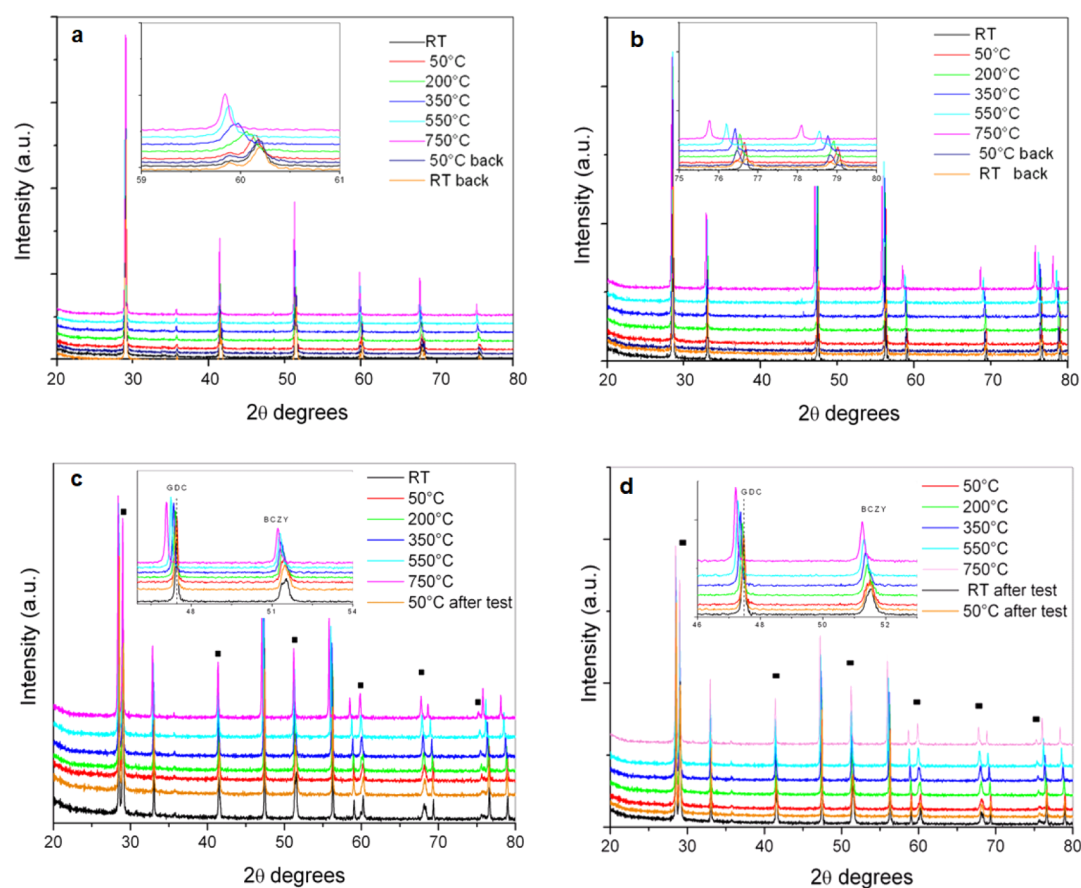


Figure 1. X-ray diffractograms recorded in 4.58% H_2/N_2 flow with a heating ramp of 10 °C/min for BCZY (a); GDC (b); and BCZY–GDC (c) and recorded in the air for BCZY–GDC (d). The inset shows details to highlight changes during the heating ramp. In (c,d) peaks belonging to the BCZY phase are indicated by (■).

Table 1. Rietveld Refinement Results of Selected Diffractograms for BCZY and for GDC Collected during Reduction and Oxidation Ramps^a

sample	temp [°C]	ramp	phase	cell parameters [Å]	pseudo cubic volume [Å ³]
BCZY	50	H_2/N_2	orthorhombic	$a = 6.1550(2), b = 6.1764(2), c = 8.6781(2)$	82.48(17)
	550	H_2/N_2	cubic	$a = 4.3657(7)$	83.21(42)
	750	H_2/N_2	cubic	$a = 4.3847(1)$	84.296(1)
	50	H_2/N_2	orthorhombic	$a = 6.1562(2), b = 6.1786(2), c = 8.6785(2)$	82.53(17)
	50	air	orthorhombic	$a = 6.1566(2), b = 6.1786(2), c = 8.6785(2)$	82.53(17)
	500	air	cubic	$a = 4.3742(1)$	83.692(3)
	750	air	cubic	nd ^b	nd
	50	air	orthorhombic	$a = 6.1555(2), b = 6.1768(2), c = 8.6810(2)$	82.51(57)
	GDC	50	H_2/N_2	cubic	$a = 5.4165(2)$
550		H_2/N_2	cubic	$a = 5.4510(81)$	161.969(5)
750		H_2/N_2	cubic	$a = 5.4830(1)$	164.837(3)
50		H_2/N_2	cubic	$a = 5.4284(1)$	159.958(3)
50		air	cubic	$a = 5.4160(1)$	158.868(2)
550		air	cubic	$a = 5.4510(1)$	161.971(5)
750		air	cubic	$a = 5.4639(1)$	163.117(5)
50		air	cubic	$a = 5.4252(1)$	159.678(2)

^aSequence of treatment: (i) ramp in H_2 (4.58%)/ N_2 starting from 50 to 750 °C and then back to 50 °C; (ii) treatment in air at 500 °C; and (iii) ramp in the air from 50 to 750 °C and then back to 50 °C. ^bWe limited the oxidation ramp for BCZY up to 500 °C since the previous studies did not show significant structural changes above this temperature.³⁸

hydroxyl groups. The signal was left to equilibrate in the atmosphere of the reaction for 30' before starting the heating ramp. The equilibrated signal at RT was used as a reference for drawing a baseline. H_2 consumption was quantified by a standard calibration procedure as already reported.⁴¹ Two consecutive TPRs were carried

out on the composite, alternating an oxidation step in the air at 900 °C for 1 h.

2.2.4. Thermogravimetric Analyses. TGA of the as-prepared samples were carried out under 4.58% H_2 in N_2 flow (100 cm^3/min) using a Q500 thermo balance (TA Instruments). The gas flow was

Table 2. Rietveld Refinement Results of Selected Diffractograms for the BCZY–GDC Composite Collected during Reduction and Oxidation Ramps^a

sample	temp [°C]	ramp	phase	cell parameters [Å]	pseudo cubic volume [Å ³]
BCZY	50	H ₂ /N ₂	orthorhombic	$a = 6.1404(3), b = 6.1695(3), c = 8.6774(5)$	82.18(20)
	550	H ₂ /N ₂	cubic	$a = 4.3702(7)$	83.468(4)
	750	H ₂ /N ₂	cubic	$a = 4.3817(1)$	84.126(4)
GDC	50	H ₂ /N ₂	orthorhombic	$a = 6.1377(2), b = 6.1675(2), c = 8.6813(2)$	82.16(21)
	50	H ₂ /N ₂	cubic	$a = 5.4179(1)$	159.036(6)
	550	H ₂ /N ₂	cubic	$a = 5.4524(1)$	162.077(6)
	750	H ₂ /N ₂	cubic	$a = 5.4793(1)$	164.500(6)
BCZY	50	H ₂ /N ₂	cubic	$a = 5.4229(1)$	159.476(6)
	50	air	orthorhombic	$a = 6.1404(3), b = 6.1707(3), c = 8.6761(4)$	82.19(19)
	550	air	cubic	$a = 4.3699(5)$	83.448(3)
	750	air	cubic	$a = 4.3802(7)$	84.04(40)
GDC	50	air	orthorhombic	$a = 6.1398(3), b = 6.1686(3), c = 8.6786(5)$	82.17(19)
	50	air	cubic	$a = 5.4181(1)$	159.050(6)
	550	air	cubic	$a = 5.4501(1)$	161.891(3)
	750	air	cubic	$a = 5.4652(1)$	163.237(6)
	50	air	cubic	$a = 5.4198(1)$	159.204(5)

^aSequence of treatment: (i) ramp in H₂ (4.58%)/N₂ starting from 50 to 750 °C and then back to 50 °C; (ii) treatment in air at 500 °C; and (iii) ramp in air from 50 to 750 °C and then back to 50 °C.

transversal to the surface of the sample. The reduction occurred in isothermal conditions at 200, 350, 550, 750, and 900 °C.

3. RESULTS AND DISCUSSION

3.1. X-ray Analysis. The structural changes of the single oxides and of BCZY–GDC composite during redox cycles were studied by in situ X-ray diffractometry. X-ray diffractograms of the samples at RT are shown in Figure S2. The obtained profiles confirmed our previous results;³⁸ GDC crystallizes in a cubic phase (*Fm3m*), while BCZY shows an orthorhombic symmetry (*Imma*). BCZY diffractogram also showed small peaks at 34, 48, and 57 2θ degrees, which were attributed to the presence of a small impurity of Y₂O₃ in the material.¹⁹ The XRD of the BCZY–GDC composite results from the overlap of the profiles of the single components.

During thermal treatment in reducing atmosphere, we observed changes in the shape and in the positions of peaks of BCZY (Figure 1a), while GDC peaks showed a gradual shift to lower 2θ angles as temperature increased without any change in their shape (Figure 1b).

BCZY underwent the first phase transition from an orthorhombic (*Imma*) structure to a trigonal phase (*R3c*) around 200 °C and then a second transition to a cubic phase (*Pm3m*) above 500 °C (Figure S3). These results well agree with previous observations collected at the synchrotron Petra III (DESY Synchrotron, Hamburg).³⁸ Table 1 shows the results of Rietveld refinement of some representative diffractograms proving that the transitions were reversible and independent on the treatment atmosphere (see also Figure S4). BCZY peaks were also observed to shift to lower 2θ angles by increasing the temperature up to 550 °C. Above this temperature, the displacement was visible only for the peaks at high angles. This result correlated with the thermal expansion of the BCZY lattice during the heating ramp. After the redox cycle, the volume of the cell returned back to the initial value.

GDC did not show modifications of the cubic symmetry during the thermal treatments in both oxidizing and reducing atmospheres, showing a shift of all peaks toward lower 2θ angles as the temperature increased (Figures 1b and S5). Below 550 °C, the shift was independent from the treatment

atmosphere and due to mechanical expansion related to the increase of temperature. Above 600 °C, we recorded a larger shift under reducing conditions since at this temperature the thermal expansion of GDC lattice occurs together with the reduction of Ce⁴⁺ to Ce³⁺, which introduces cations of larger size into the structure of GDC. TPR and TGA analyses confirmed the reduction of the oxide above 600 °C.

Figure 1c,d and Table 2 summarize the XRD analyses for the BCZY–GDC composite during the thermal treatment under reducing and oxidizing atmosphere, respectively. Under both conditions, thermal behavior reflected that of bare components: GDC as well as BCZY phases showed peak shift to lower 2θ angles up to 750 °C, with a larger displacement for peaks of GDC exposed to reducing atmosphere at high temperatures (above 600 °C). However, at 750 °C, the cell parameter of the GDC lattice in the composite was slightly smaller than that of the single oxide (5.4793 vs 5.4830 Å) probably because of a minor contribution of the reduction process to the thermal expansion. The cooling to RT restored the initial profile, leaving the two phases in the composite structurally unaltered.

To summarize, diffraction data indicates that BCZY underwent two phase transitions during the thermal treatment either in an oxidizing or reducing atmosphere. These structural changes were reversible and took place together with thermal expansion that reached its maximum at 750 °C. The thermal behavior of the single phase was the same as that observed for the phase in the composite. GDC, either as single phase or in the composite, did not change its structure during the thermal treatments, but a lattice expansion occurred whose entity depended on the treatment atmosphere. The maximum thermal expansion was obtained in reducing environment at 750 °C due to the additional effect of Ce⁴⁺ reduction. Under such operating conditions, thermal expansion of GDC in the composite was smaller, suggesting that the reduction of Ce⁴⁺ in GDC was hindered by the co-presence of BCZY.

A perusal of the results reported in Tables 1 and 2 reveals that the final cell parameters of BCZY and GDC single oxides obtained after the ramps of reduction and oxidation were slightly larger than those measured at the beginning of thermal

treatment, suggesting tiny structural and compositional changes undergone by the single components during redox cycles (see Figure S5 and related comment). Moreover, complete reversibility of the thermal behavior of BCZY–GDC was observed, which can be associated with high stability of the composite.³⁸

3.2. Raman Analysis. To gain insights into the role of interfacial properties of the two oxides and into the nature of their interaction in the composite, we performed in situ Raman temperature-programmed redox experiments. Raman analysis is in fact a powerful technique to investigate the local short distance structural properties and the defects arrangement of ceria-based materials^{42,43} and to follow structural changes of protonic conductor perovskite oxides^{27,29,44}

Figure 2 shows the Raman spectra of the as-prepared BCZY, GDC, and BCZY–GDC (see the Supporting Information for details in the analysis, Figures S6–S8 and Table S1).

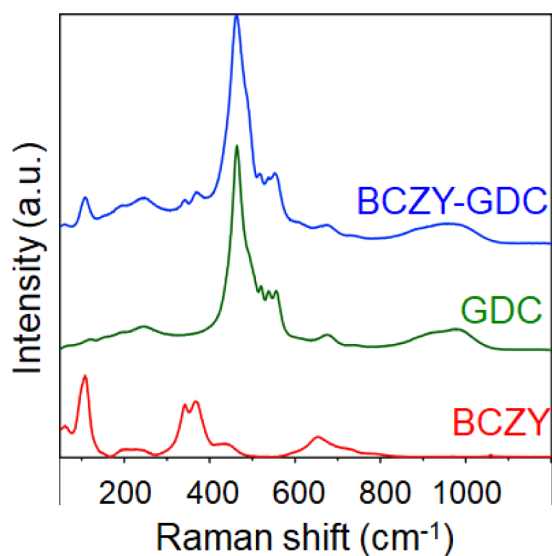


Figure 2. Comparison of normalized Raman spectra of BCZY, GDC, and BCZY–GDC.

BCZY profile is characterized by peaks at about 61, 108, 218, 341, 367, 434, and 654 cm^{-1} . The tiny peak at 1056 cm^{-1} (see Figure S8) is attributed to OH groups embodied into the lattice.⁴⁴ The peaks are typical of a rhombohedral structure as reported by Tu et al.²⁷ The peaks at 108, 341, and 367 cm^{-1} could be attributed to the three E_g modes of the $R3c$ -phase.^{27,28,45} The difference in the peaks position compared to the reference is due to the specific composition analyzed in this study. The bands in the range of 340–370 cm^{-1} , which were associated with the X–O ($X = \text{Ce}, \text{Zr}, \text{Y}$) stretching modes, are in fact sensitive to the cerium content in the BCZY system. The weak shoulder at 434 cm^{-1} is attributed to a symmetrical radial breathing mode of the six oxygen ions around Ce^{4+} in the perovskite structure. The band in the range of 550–900 cm^{-1} could be related to vibration stretching modes of Zr–O bonds.⁴⁶ The increase of the intensity/frequency of this band has been related to the transition from rhombohedral to cubic phase.²⁷ On the other hand, the presence of this band in cubic perovskites could be indicative of the presence of oxygen vacancies into the lattice.⁴⁷

Raman results contrast with XRD findings which showed the formation of stable *Imma* orthorhombic structure at RT. The

structure of cerates–zirconates at RT depends on their composition and degree of hydration.⁴⁸ Many studies reported diagrams that rationalize the structural evolution of BCZ and/or BCZY according to the amount of cerium.^{27,29} Generally, for molar yttrium content of 0.1–0.2, a threshold value of cerium molar content is identified above which the orthorhombic or monoclinic structure would be stabilized. This value is in the range of 0.6–0.7 depending on the characterization techniques used. Neutron and synchrotron XRD studies reported a monoclinic structure for a composition identical to that under investigation.²⁹ On the other hand, the rhombohedral structure detected here agrees with the diagram designed through Raman studies²⁷ for $\text{Ba}(\text{Zr}_{0.8-x}\text{Ce}_x\text{Y}_{0.20})\text{O}_{2.9}$ compositions. The sample studied in this work contains an amount of cerium which falls within the range of critical values for the assessment of BCZY phase transition from rhombohedral to orthorhombic. The discrepancy of results between Raman and XRD analyses can be justified based on a higher sensitivity of Raman spectroscopy to the detection of structural transitions compared to X-ray diffractometry. On the other hand, our results are also compatible with the Raman potentiality of short-to-medium structural analysis to identify microdomains of different composition and higher symmetry, which may be present in the oxide.

GDC spectrum shows small and overlapped peaks at 116, 167, 193, and 246 cm^{-1} , an asymmetric intense band at 463 cm^{-1} , with a shoulder at 486 cm^{-1} , a series of peaks in the range of 520–610 cm^{-1} , a less intense peak at 674 cm^{-1} , and a broad band around 807–1088 cm^{-1} . According to the literature, the most intense peak is due to the F_{2g} symmetric vibration mode of Ce–O bond in an eightfold configuration, which is typical of CeO_2 fluorite compounds. Peaks at 248 cm^{-1} and those at 522, 538, and 557 cm^{-1} are instead related to the introduction of Gd into the fluorite structure with the creations of vacancies within the Gd coordination sphere.^{49,50} Recently, DFT calculation and experimental studies demonstrated that the band at about 560 cm^{-1} resulted from the stretching vibration of O atom between M^{3+} and Ce^{4+} ions near oxygen vacancies.⁵¹ Therefore, it was correlated to the existence of intrinsic vacancies due to non-stoichiometric conditions of the oxides (substitution of Ce^{4+} with Ce^{3+} cations).⁵² The peak above 600 cm^{-1} was attributed to the formation of a ReO_8 -type complex due to the substitution of Ce by Gd, with no oxygen vacancies, but participating in the formation of Frenkel oxygen defects.⁵³ The band above 800 cm^{-1} was related to the presence of peroxides and superoxides.⁵⁴

In the spectrum of the BCZY–GDC composite, we observed the typical peaks of both BCZY and GDC components; however, the peaks related to the GDC were more intense. This is consistent with the composition of the material (that contains 54 wt % of GDC) and with different adsorption of the two oxides (Figures S7 and S8). The spectrum shows some differences from those calculated by the combination of the spectra of the single components as observable in Figure S9; these differences are mainly found in the relative intensity of the bands of the two components and in the shape of bands linked to the presence of defects and vacancies. The intensity ratios between relevant bands are summarized in Table S2. In more detail: (1) the ratio between intensity (I) area of bands at ~ 560 and ~ 463 cm^{-1} ($R = I_{560}/I_{463}$), which is often referred to as a measure of the oxygen vacancies and of the reducibility of rare earth-doped ceria

oxides,^{51,55} resulted in being smaller for the composite ($R = 0.1$) compared to that for pure GDC ($R = 0.23$), thus indicating a lower reduction of the former. (2) The tiny differences in the range of $460\text{--}580\text{ cm}^{-1}$ existing between pure GDC and the composite could be due to an alteration of the electronic environment of vacancies due to the presence of BCZY–GDC interfaces. (3) The attenuation of the peaks belonging to BCZY in the composite (at 108 , $339\text{--}370$, and at 654 cm^{-1}) could imply an alteration of the perovskite symmetry because of the interaction with GDC.⁵⁶ In conclusion, the Raman spectrum of BCZY–GDC is not the result of the mere sum of the spectra of the single components, and it reveals the occurrence of a peculiar configuration of defects likely related to the interfacial properties of the composite.

Figure 3 shows the results of Raman temperature-programmed analysis carried out on BCZY, GDC, and BCZY–GDC, either in reducing atmosphere (4.58% H_2 in N_2) and in the air after an oxidation step at $600\text{ }^\circ\text{C}$. For all samples, the spectra show a decrease of the intensity of the bands with the increase of temperature. Generally, in Raman analyses, an increase in temperature leads to a broadening and

a reduction of band intensity because of the increase in disorder due to thermal movement. In addition, all bands move toward lower Raman shift due to the decreasing energy necessary to excite vibrations along progressively looser bonds.^{31,53}

Another commonality between all samples is that the spectra acquired under reduced conditions show bands of lower intensity than the spectra collected in air which is probably due to the different absorption properties of the sample in the two atmospheres.⁵⁷ Under reducing atmosphere, the thermal quenching of bands was also faster, especially for GDC and for the composite. Reduced samples were darkish and therefore the majority of the excitation laser and scattering light is expected to be absorbed by the sample, rather than contribute to the Raman signal. Moreover, with the increase of oxygen vacancies within the material, the concentration of metal cations increases compared to that of oxygen ions. This leads to a decrease in polarization and an increase in surface reflectivity which contribute to decrease the intensity of the Raman bands.⁵⁸ The effect of the thermal radiation of the oxides caused the signal to become very low and noisy especially above $680\text{ }^\circ\text{C}$, thus making it almost impossible to obtain information regarding the evolution of defects and changes of phases above $600\text{ }^\circ\text{C}$. Bearing in mind all of the above limitations, the comparison among samples were carried out by the sequences of normalized spectra (see Figure S10, S11 and S12 for BCZY, GDC, and BCZY–GDC, respectively).

In order to understand the changes observed for BCZY–GDC composite, we first investigated the thermal behavior of single components. For both BCZY and GDC, the main spectra modifications were observed in the first stage of the heating ramp and above $400\text{ }^\circ\text{C}$. Tables 3 and 4 summarize the results for BCZY and GDC, respectively.

The results in Table 3 are consistent with the previous studies that reported a change in the spectra in the range of $650\text{--}800\text{ }^\circ\text{C}$, corresponding to a phase transition from rhombohedral to cubic of the BCZY structure.^{27,28} It is worth pointing out that in our case the transition was gradual and started already at around $500\text{ }^\circ\text{C}$.

From Table 4, it is clear that the thermal evolution of the GDC spectrum is strongly correlated to the reorganization of surface defects and the formation of oxygen vacancies. The bands linked to vibrational modes involving oxygen vacancies decreased with different rates compared to the main peak at around 460 cm^{-1} . This limited the possibility of a quantitative analysis of the reduction process.⁵² However, its qualitative analysis was estimated by normalizing the spectra collected above $600\text{ }^\circ\text{C}$ and following the intensity ratio between the bands at ~ 570 and $\sim 463\text{ cm}^{-1}$. The values of this parameter (I_{570}/I_{460}) were higher for the spectra collected in hydrogen than those measured in air (Figure 4). Furthermore, in H_2 they reached a plateau because the reduction process caused an increase of intensity of the band at $570\text{--}600\text{ cm}^{-1}$ contrasting the opposite effect of temperature. On the other hand, during the air heating ramp, the intensity of the bands decreased simultaneously but with different magnitude, which led to a linear increase in the I_{570}/I_{460} ratio.

The evolution of the BCZY–GDC Raman spectrum during the heating treatments reflected the evolution of the spectra of the single components in air and in hydrogen flow (Figures 3C and S12). However, some of the bands related to GDC overlapped with those of BCZY. For example, above $400\text{ }^\circ\text{C}$, spectrum modifications in the range $500\text{--}650\text{ cm}^{-1}$ were

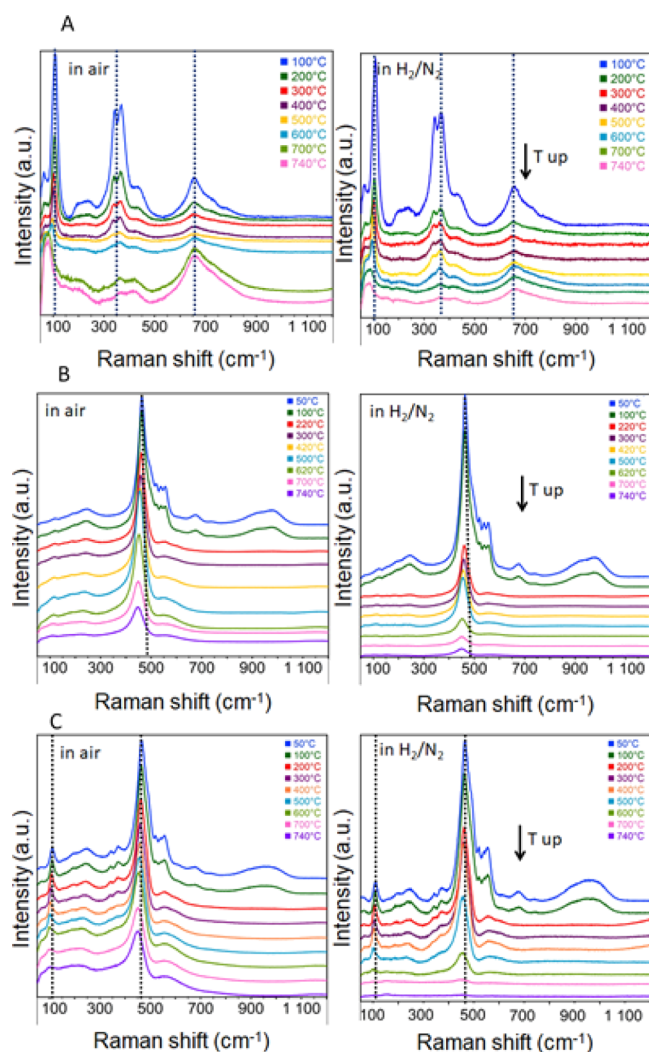


Figure 3. Raman spectra of single components during a heating ramp in different atmospheres of reaction: BCZY (A), GDC (B), and BCZY–GDC (C).

Table 3. Trend of Main Relative Changes of BCZY Bands during Thermal Treatments

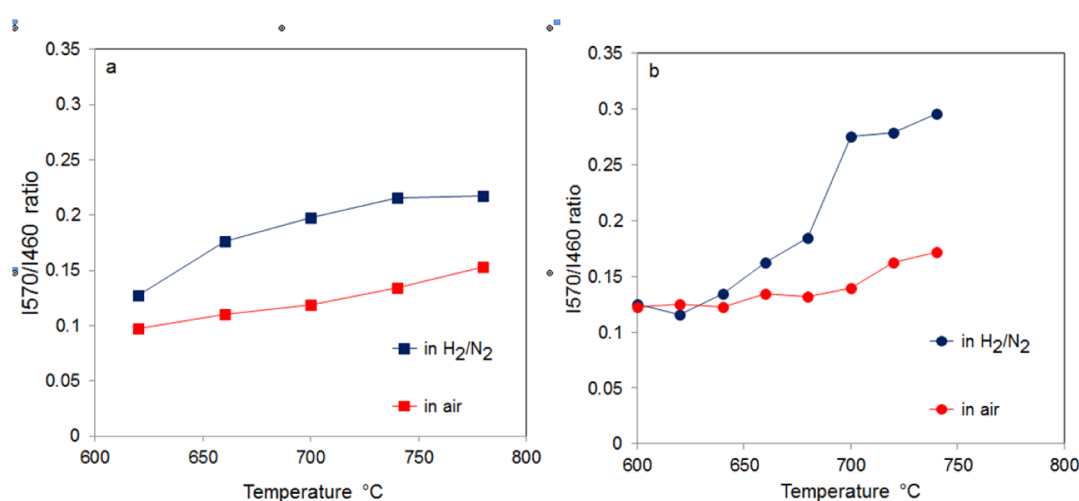
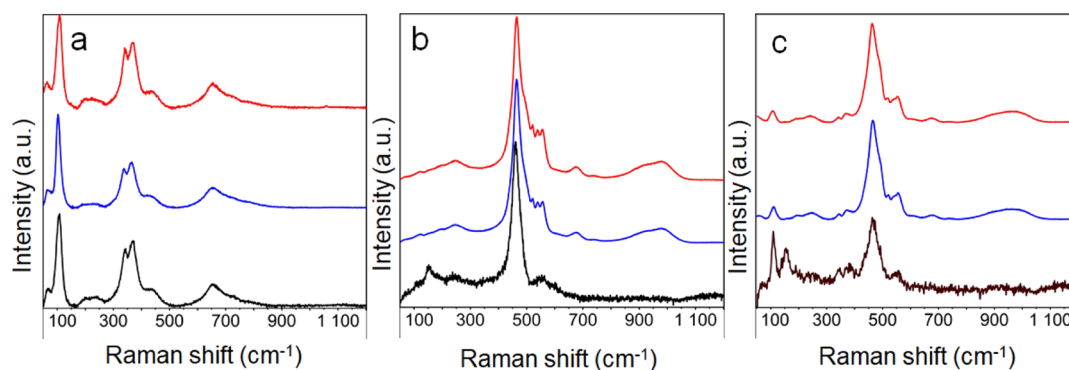
temp [°C]	BCZY bands ^a [cm ⁻¹]			
	~108	~340–370	~420–430	~650
50–260	negligible changes	slight decrease of intensity	negligible changes	negligible changes
260–400	negligible changes	negligible changes	negligible changes	negligible changes
400–600	shift to lower wavenumbers	changes in the relative intensity, convergence to single peak at 360 cm ⁻¹	negligible changes	increase intensity
600–740	fading and disappearance	decrease intensity	negligible changes	high intensity, slight shift to higher wavenumbers

^aSimilar behavior in air and in H₂.

Table 4. Trend of Main Relative Changes of GDC Bands during Thermal Treatments

temp [°C]	GDC bands ^a [cm ⁻¹]				
	~200	~463	~540–590	~680	~900–1000
50–260	negligible changes	very little broadening	higher in H ₂ , rapid decrease	fading to vanish	fading to vanish
260–500	slight increase	slight broadening	slight increase	Disappeared	disappeared
500–740	increase of background above 680 °C appearance of peak at 150 cm ⁻¹ in H ₂	broadening	increasing, more in H ₂	Disappeared	disappeared

^aFaster decrease in H₂; heat-related behavior depending on the type of bands.

Figure 4. Evaluation of I_{570}/I_{460} ratio under reducing and oxidizing heating ramp for (a) GDC and (b) BCZY-GDC.Figure 5. Raman spectra of oxidized (a) BCZY, (b) GDC, and (c) BCZY-GDC before (blue) and after (red) a redox cycle. Spectra in black are related to the samples after the ramp in H₂/N₂.

attributed both to the phase transition of BCZY and, under reduced conditions, also to the introduction of surface oxygen vacancies. This mainly involves the release of interstitial oxygen associated to MO_x defects in GDC⁵³ and the surface reduction

of Ce⁴⁺ (see Temperature-Programmed Analyses section). Taking this into account, we used the ratio I_{570}/I_{463} for a qualitative estimation of the reduction process in the composite, as done for the GDC (Figure 4b).

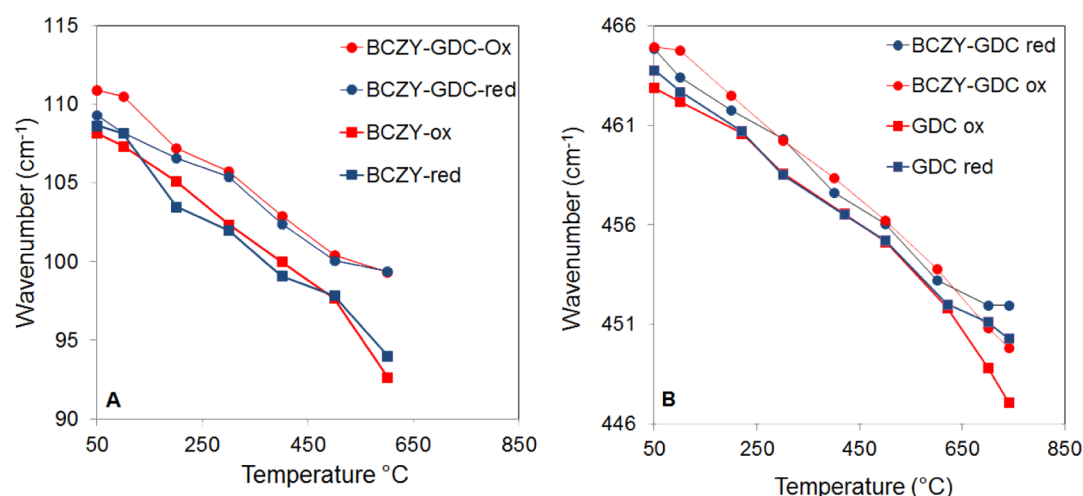


Figure 6. Trends of the shift for the peak at 108 cm^{-1} (A) and peak at $\sim 464\text{ cm}^{-1}$ (B) in the single oxides and in the composite.

For all samples, we followed the cooling ramps both in air and in H_2/N_2 (results not shown). The spectra collected in oxidizing conditions overlapped with those recorded during the heating ramp. This suggests that the structural changes were mainly related to the thermal expansion of the samples and were reversible. On the other hand, the thermal treatment in reducing condition led to a substantial modification of the final spectrum at RT in the case of GDC and BCZY–GDC.

Figure 5 showed the effect of a redox cycle on the materials investigated. In BCZY, we registered some irreversible modifications in the intensity of bands and in their mutual ratio (see Figure 5a: bands at $340\text{--}370$ and $\sim 670\text{ cm}^{-1}$ are higher in comparison to the peak at around $\sim 108\text{ cm}^{-1}$; moreover this latter band shifted to slightly higher wavenumbers). This suggests that the redox thermal treatment affected the sub-lattice of A and B cations favoring a higher symmetry of the lattice. In GDC (Figure 5b), the intensity of peaks after reduction was very low due to the high absorbance of the reduced oxide, with the band at $560\text{--}600\text{ cm}^{-1}$ being almost a shoulder of the highest peak at 461 cm^{-1} . It was possible to see the presence of a tiny peak at 150 cm^{-1} . No appropriate assignment could be found in the literature for this peak; however, the signal was clearly correlated with structural changes caused by the reduction. After re-oxidation at $600\text{ }^\circ\text{C}$, the spectrum was similar to that of the initial oxidized sample but with a higher intensity of the bands at $520\text{--}560$ and at 676 cm^{-1} and of those centered at 943 cm^{-1} . All these bands were related to the presence of structural defects and oxygen vacancies.^{52,53,59} The fact that their intensity increased after a redox cycle suggests that the oxide remained partially reduced.

In BCZY–GDC, the thermal treatment under reducing condition led to a transformation of the final spectrum at RT, with a strong attenuation of the peaks related to GDC in comparison to those attributable to BCZY. The re-oxidation of the sample at $600\text{ }^\circ\text{C}$ allowed recovering of the initial spectrum (Figure 5c).

The medium-short distance structural changes detected in the bare BCZY and GDC after the redox cycle were completely reversible in the composite, suggesting that BCZY and GDC composite components synergistically counteracted their transformations mainly due to the reduction process. We investigated the dynamics of this interaction by following the shift of the main peak of the fluorite structure (peak at $\sim 463\text{ cm}^{-1}$) and of the orthorhombic structure (peak at $\sim 108\text{ cm}^{-1}$)

of BCZY–GDC. In fact, any difference from the general trend of this parameter, which is related to the thermal expansion of materials, should give information on the occurrence of interfering phenomena, such as reduction and structural changes, and about their impact on the involved structures.^{55,59}

Figure 6A shows that the displacement of the peak at $\sim 108\text{ cm}^{-1}$ followed the same trend both in hydrogen and in air, but it was less pronounced in the BCZY–GDC composite than in pristine BCZY. Moreover, in the composite spectra, we observed a phenomenon of anti-crossing at $500\text{ }^\circ\text{C}$, that is, the softening of the mode corresponding to the band at 108 cm^{-1} decreased abruptly. The accurate description of the anti-crossing phenomenon, which is usually attributed to the strong interaction between two different modes, would require further spectroscopic analyses, and it is out of the scope of this study.⁶⁰ However, considering that at $500\text{ }^\circ\text{C}$ a symmetrization of the perovskite was observed, we concluded that anti-crossing in the softening of the band at 108 cm^{-1} could be taken as a descriptor of the $R\bar{3}c \rightarrow Pm\bar{3}m$ phase transition for BCZY–GDC. This transition implies a contraction of the BCZY lattice; the different trend observed for the BCZY single-phase material suggests that the thermal expansion of the BCZY lattice in the composite is hindered by the presence of GDC, and the effect is more relevant when the structure becomes cubic.

Figure 6B shows that the peak shift at $\sim 461\text{ cm}^{-1}$ followed a similar trend for both GDC and BCZY–GDC, regardless of the treatment atmosphere, up to $600\text{ }^\circ\text{C}$. At this temperature, we observed anti-crossing phenomena for both GDC and BCZY–GDC when the atmosphere of treatment is diluted H_2 . Above $600\text{ }^\circ\text{C}$, there was a decrease in the extent of the shift with a greater effect on the GDC than on the composite. A deeper spectroscopic analysis would be required to describe in more detail this phenomenon; however, we put forward an explanation based on the recent theoretical studies.^{54,61} Muhich⁶¹ proposed that the reduction of Ce^{4+} to the larger Ce^{3+} cation is not the main cause of ceria lattice expansion. The elongation of $\text{Ce}^{3+}\text{--O}^{2-}$ bond is counterbalanced by the concomitant contraction of neighboring $\text{Ce}^{4+}\text{--O}^{2-}$ bonds and the long-distance expansion is rather due to an outward relaxation of Ce^{4+} neighboring the vacancy. This originates from the non-counterpoised attractive forces induced on Ce^{4+} cations by O anions 180° opposite to the vacancy. This model agrees with recent calculations that demonstrated that a blue

shift of the F_{2g} Raman mode in CeO_{2-x} is expected if the lattice constant is not allowed to relax after defect creation.⁵⁴ Considering that the shift of the peak at 461 cm^{-1} accounts for the contribution due to the reduction of cerium,⁵⁵ the anti-crossing behavior observed in the reducing condition should be correlated with the process of reduction. Under the experimental conditions, the formation of oxygen vacancies should have a compensatory effect on the softening of the mode caused by thermal expansion. In this view, we attributed the differences in the trend between the two materials to a different number of vacancies.

From these results, it was possible to identify a critical temperature range ($550\text{--}750\text{ }^\circ\text{C}$) where the interaction between GDC and BCZY made GDC to thermally stabilize against the reaction atmosphere. Above $550\text{ }^\circ\text{C}$, the BCZY phase is cubic, and this structure can interact strongly with the cubic lattice of GDC, giving rise to more resistant and flexible interfacial bonds to comply with the effect of redox processes. These findings are consistent with the results of our recent study through in situ synchrotron XRD characterization which demonstrated that, at high temperature, in humidified H_2 , there is a synergistic effect between GDC and BCZY in the composite. This induces thermal expansion of the individual components in favor of greater reciprocal compatibility to thermomechanical stress.³⁸

The redox flexibility and thermomechanical properties of this material would allow contrasting the strains induced by the expansion of ceria lattice in reducing conditions, especially when applied as a structured component in devices such as fuel cells and membranes.

3.3. Temperature-Programmed Analyses. XRD and Raman characterizations suggested that the high thermal stability and the reversibility of BCZY–GDC redox behavior was linked to lower propensity of GDC of being reduced in the presence of BCZY. In order to verify this hypothesis and estimate the reducibility of the materials we carried out TGA and TPR measurements on the samples under 4.58% H_2 in N_2 atmosphere.

Figure 7 shows the results of TPR measurements. GDC and BCZY–GDC profiles show a small peak around $450\text{ }^\circ\text{C}$ related to the reduction of surface sites and a large signal at $750\text{--}800\text{ }^\circ\text{C}$, attributable to the bulk reduction of Ce^{4+} to Ce^{3+} into the GDC lattice.

TPR profile of BCZY shows a peak at about $500\text{ }^\circ\text{C}$ and two other small peaks at a higher temperature, which are

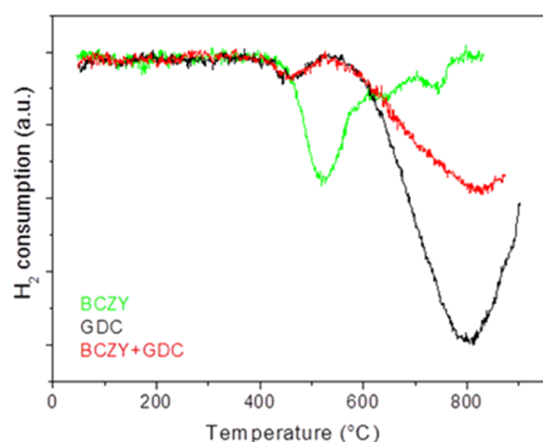


Figure 7. TPR profiles of BCZY, BCZY–GDC, and GDC.

attributable to reduction of Ce^{4+} to Ce^{3+} in the BCZY lattice. TPR profiles are congruent with TGA results (Figure S13). The quantitative results of TPR and TG analyses are reported in Table 5. Because of the different configuration of the two

Table 5. Summary of TGA and TPR Results

samples	O_2 released from TGA [$\mu\text{mol/g}$]	H_2 consumed in TPR [$\mu\text{mol/g}$] ^a
GDC	326	1624
BCZY	157	193
BCZY–GDC	159	622

^aCorresponding to a reduction of Ce^{4+} to Ce^{3+} of 66, 18, and 16% from top to bottom.

experiments the consumption of H_2 measured during TPR experiments is not directly comparable with the amount estimable from the TGA profiles. However, qualitatively the results of the two analyses showed the same behavior, that is, the degree of reduction of the composite was lower than what could be expected (16 vs 53%) from the reduction degree of the single components. The stability of the composite toward a redox treatment and the reproducibility of results have been proved by performing two successive TPRs after an isothermal oxidation step at $900\text{ }^\circ\text{C}$ (Figure S14).

Therefore, it is established that the reduction of GDC in the BCZY–GDC composite is inhibited due to the interaction between the two components. The mechanism of interaction is summarized in Figure 8 and the equilibrium at the interface can be described by the reactions of Scheme 1. At high temperature, the incorporation of hydrogen as OH groups into the cubic lattice of BCZY and the simultaneous reduction of Ce^{4+} to Ce^{3+} with the formation of water may lead in the

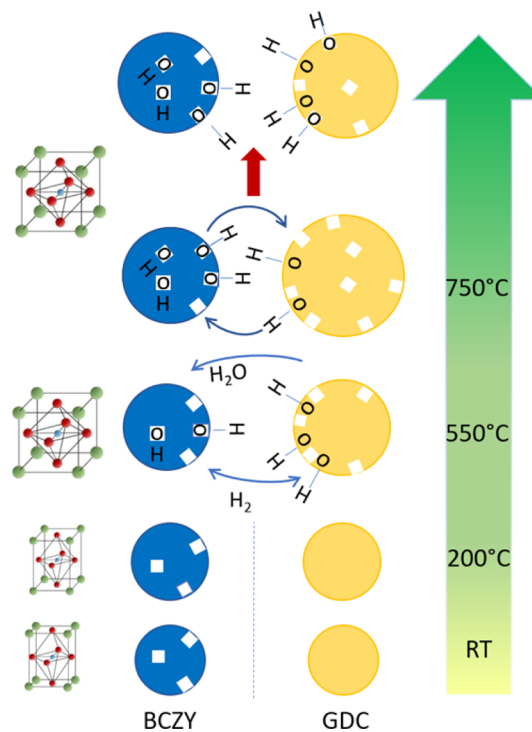
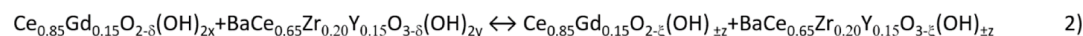


Figure 8. Representation of transformation and interaction of GDC and BCZY in the composite.

Scheme 1. Reactions Describing the Redox Process Occurring at the BCZY–GDC Interface, Where OH Groups Can Be H₂ or H₂O Adsorbed and $\zeta < \delta$



interfacial zone to a local composition of adsorbed gases which shifts the equilibrium of reduction to the left.

This mechanism is supported by the fact that ceria reduction by H₂ involves the formation of hydroxyl groups as intermediates. Moreover, the reactivity of these latter depends on the configuration of vacancies and on the presence of strain in the oxide.^{62,63}

4. CONCLUSIONS

This is the first study that focuses specifically on the redox behavior of the BCZY–GDC dual-phase ceramic and its thermal and mechanical stability. BCZY–GDC showed full redox reversibility in comparison to the single oxides; its reduction involved mainly GDC, which was less reducible in the presence of BCZY, thus allowing a higher thermal and mechanical robustness of the composite. Different techniques of analysis (TPR, TGA, in situ Raman, and in situ XRD) under temperature-programmed conditions revealed that the interaction between the single components occurred at the nanoscale, impacting the redox behavior and the thermal resistance of BCZY–GDC especially at high temperature. At high temperatures and under reducing atmosphere, structural changes in the BCZY and the introduction of oxygen vacancies in the GDC lattice by Ce⁴⁺ reduction act synergistically, determining interfacial processes able to limit the mechanical strains induced by the expansion of lattices with temperature and reduction.

This work highlights the importance of fundamental studies on redox behavior of perovskite–fluorite composites since they can reveal the occurrence of specific synergies between their components during operating conditions. This unexpected behavior would help develop engineered materials with enhanced functionalities in high-temperature redox applications.

■ ASSOCIATED CONTENT

SI Supporting Information

The Supporting Information is available free of charge at <https://pubs.acs.org/doi/10.1021/acsaem.0c01589>.

Scheme of thermal treatments during Raman experiments; XRD of the samples before thermal treatments; X-ray diffractograms of BCZY recorded at different temperatures in H₂ flow and BCZY and GDC recorded at different temperatures in air flow; analysis of BCZY, GDC, and BCZY-GDC Raman spectrum before the thermal treatments; comparison between Raman spectrum of measured BCZY-GDC composite and that calculated from the weighted sum of the spectra recorded for the single GDC and BCZY; comparison of Raman spectra of BCZY, GDC, and BCZY-GDC; TGA profile for GDC, BCZY, and BCZY-GDC; double TPR on BCZY-GDC; intensity and position of peaks of the investigated specimens as calculated from fitting analysis; and comparison of typical Intensity Area peaks for the investigated samples (PDF)

■ AUTHOR INFORMATION

Corresponding Author

Marta Boaro – Dipartimento Politecnico di Ingegneria e Architettura, University of Udine, 33100 Udine, Italy;
 orcid.org/0000-0002-6853-2965; Email: marta.boaro@uniud.it

Authors

Cecilia Mortalò – Istituto di Chimica della Materia Condensata e di Tecnologie per l'Energia (ICMATE), Consiglio Nazionale delle Ricerche (CNR), 35127 Padova, Italy

Elena Rebollo – Istituto di Chimica della Materia Condensata e di Tecnologie per l'Energia (ICMATE), Consiglio Nazionale delle Ricerche (CNR), 35127 Padova, Italy

Valentina Zin – Istituto di Chimica della Materia Condensata e di Tecnologie per l'Energia (ICMATE), Consiglio Nazionale delle Ricerche (CNR), 35127 Padova, Italy

Eleonora Aneggi – Dipartimento Politecnico di Ingegneria e Architettura, University of Udine, 33100 Udine, Italy

Monica Fabrizio – Istituto di Chimica della Materia Condensata e di Tecnologie per l'Energia (ICMATE), Consiglio Nazionale delle Ricerche (CNR), 35127 Padova, Italy;

 orcid.org/0000-0003-2257-8375

Alessandro Trovarelli – Dipartimento Politecnico di Ingegneria e Architettura, University of Udine, 33100 Udine, Italy;

 orcid.org/0000-0002-1396-4031

Complete contact information is available at:
<https://pubs.acs.org/10.1021/acsaem.0c01589>

Author Contributions

The manuscript was written through contributions of all authors. All authors have given approval to the final version of the manuscript.

Notes

The authors declare no competing financial interest.

■ ACKNOWLEDGMENTS

This work has been partially funded by the Italian Ministry of Economic Development —Italia National Research Council Agreement 2015–2017 “Ricerca di Sistema Elettrico Nazionale”; UNIUD is also grateful to MIUR to sustain partially this research (PRIN, BIOSOFOC), to Prof. Carla de Leitenburg (DPIA, UNIUD) for her assistance during in situ XRD experiments.

■ REFERENCES

- (1) Abdin, Z.; Zafaranloo, A.; Rafiee, A.; Mérida, W.; Lipiński, W.; Khalilpour, K. R. Hydrogen as an energy vector. *Renewable Sustainable Energy Rev.* **2020**, *120*, 109620.
- (2) International Energy Agency. *The Future of Hydrogen*, <https://www.iea.org/reports/the-future-of-hydrogen>, 2019.
- (3) Hydrogen Council. *How Hydrogen Empowers the Energy Transition*, <https://www.hydrogencouncil.com>, report 2017.
- (4) Marrony, M. *Protons Ceramic Conductors*; Taylor & Francis Group, LLC, Pan Stanford Publishing: USA, 2016.

- (5) Iwahara, H.; Asakura, Y.; Katahira, K.; Tanaka, M. Prospect of hydrogen technology using proton-conducting ceramics. *Solid State Ionics* **2004**, *168*, 299–310.
- (6) Kim, J.; Sengodan, S.; Kim, S.; Kwon, O.; Bu, Y.; Kim, G. Proton conducting oxides: A review of materials and applications for renewable energy conversion and storage. *Renewable Sustainable Energy Rev.* **2019**, *109*, 606–618.
- (7) Hossain, S.; Abdalla, A. M.; Jamain, S. N. B.; Zaini, J. H.; Azad, A. K. A review on proton conducting electrolytes for clean energy and intermediate temperature-solid oxide fuel cells. *Renewable Sustainable Energy Rev.* **2017**, *79*, 750–764.
- (8) Duan, C.; Tong, J.; Shang, M.; Nikodemski, S.; Sanders, M.; Ricote, S.; Almansoori, A.; O'Hayre, R. Readily processed protonic ceramic fuel cells with high performance at low temperatures. *Science* **2015**, *349*, 1321–1326.
- (9) Duan, C.; Kee, R.; Zhu, H.; Sullivan, N.; Zhu, L.; Bian, L.; Jennings, D.; O'Hayre, R. Highly efficient reversible protonic ceramic electrochemical cells for power generation and fuel production. *Nat. Energy* **2019**, *4*, 230–240.
- (10) Wang, H.; Wang, X.; Meng, B.; Tan, X.; Loh, K. S.; Sunarso, J.; Liu, S. Perovskite-based mixed protonic–electronic conducting membranes for hydrogen separation: Recent status and advances. *J. Ind. Eng. Chem.* **2018**, *60*, 297–306.
- (11) Hashim, S. S.; Somalu, M. R.; Loh, K. S.; Liu, S.; Zhou, W.; Sunarso, J. Perovskite-based proton conducting membranes for hydrogen separation: A review. *Int. J. Hydrogen Energy* **2018**, *43*, 15281–15305.
- (12) Medvedev, D.; Brouzgou, A.; Denim, A.; Tsiakaras, P. In *Advances in Medium and High Temperature Solid Oxide Fuel Cell Technology*; Aricò, A. S., Boaro, M., Eds.; Springer Nature: Cham, Switzerland, 2017; Chapter 3, Vol. 574.
- (13) Singh, K.; Kannan, R.; Thangadurai, V. Perspective of perovskite-type oxides for proton conducting solid oxide fuel cells. *Solid State Ionics* **2019**, *339*, 114951.
- (14) Tao, Z.; Yan, L.; Qiao, J.; Wang, B.; Zhang, L.; Zhang, J. A review of advanced proton-conducting materials for hydrogen separation. *Prog. Mater. Sci.* **2015**, *74*, 1–50.
- (15) Rashid, N. L. R. M.; Samat, A. A.; Jais, A. A.; Somalu, M. R.; Mughtar, A.; Baharuddin, N. A.; Wan Isahak, W. N. R. Review on zirconate-cerate-based electrolytes for proton-conducting solid oxide fuel cell. *Ceram. Int.* **2019**, *45*, 6605–6615.
- (16) Huang, J.; Zhang, L.; Wang, C.; Zhang, P. CYO–BZCYO composites with enhanced proton conductivity: Candidate electrolytes for low-temperature solid oxide fuel cells. *Int. J. Hydrogen Energy* **2012**, *37*, 13044–13052.
- (17) Medvedev, D.; Maragou, V.; Pikalova, E.; Demin, A.; Tsiakaras, P. Phase formation and properties of composite electrolyte $\text{BaCe}_{0.8}\text{Y}_{0.2}\text{O}_{3-\delta}$ – $\text{Ce}_{0.8}\text{Gd}_{0.2}\text{O}_{1.9}$ for intermediate temperature solid oxide fuel cells. *J. Power Sources* **2013**, *221*, 217–227.
- (18) Ivanova, M. E.; Escolástico, S.; Balaguer, M.; Palisaitis, J.; Sohn, Y. J.; Meulenbergh, W. A.; Guillon, O.; Mayer, J.; Serra, J. M. Hydrogen separation through tailored dual phase membranes with nominal composition $\text{BaCe}_{0.8}\text{Eu}_{0.2}\text{O}_{3-\delta}$ – $\text{Ce}_{0.8}\text{Y}_{0.2}\text{O}_{2-\delta}$ at intermediate temperatures. *Sci. Rep.* **2016**, *6*, 34773. , and reference therein
- (19) Rebollo, E.; Mortalò, C.; Escolástico, S.; Boldrini, S.; Barison, S.; Serra, J. M.; Fabrizio, M. Exceptional hydrogen permeation of all-ceramic composites robust membranes based on $\text{BaCe}_{0.65}\text{Zr}_{0.20}\text{Y}_{0.15}\text{O}_{3-\delta}$. *Energy Environ. Sci.* **2015**, *8*, 3675–3686.
- (20) Montaleone, D.; Mercadelli, E.; Escolástico, S.; Gondolini, A.; Serra, J. M.; Sanson, A. All-ceramic asymmetric membranes with superior hydrogen permeation. *J. Mater. Chem. A* **2018**, *6*, 15718–15727.
- (21) Mortalò, C.; Rebollo, E.; Escolástico, S.; Deambrosio, S.; Haas-Santo, K.; Rancan, M.; Dittmeyer, R.; Armelao, L.; Fabrizio, M. Enhanced sulfur tolerance of $\text{BaCe}_{0.65}\text{Zr}_{0.20}\text{Y}_{0.15}\text{O}_{3-\delta}$ – $\text{Ce}_{0.85}\text{Gd}_{0.15}\text{O}_{2-\delta}$ composite for hydrogen separation membranes. *J. Membr. Sci.* **2018**, *564*, 123–132.
- (22) Zhu, B.; Fan, L.; Lund, P. Breakthrough fuel cell technology using ceria-based multi-functional nanocomposites. *Appl. Energy* **2013**, *106*, 163–175.
- (23) Malavasi, L.; Tealdi, C.; Ritter, C.; Pomjakushin, V.; Gozzo, F.; Diaz-Fernandez, Y. Combined neutron and synchrotron X-Ray diffraction investigation of $\text{BaCe}_{0.85-x}\text{Zr}_x\text{Y}_{0.15}\text{O}_{3-\delta}$ ($0.1 \leq x \leq 0.4$) protons conductors. *Chem. Mater.* **2011**, *23*, 1323–1330.
- (24) Tao, S. W.; Irvine, J. T. S. A stable, easily sintered proton-conducting oxide electrolyte for moderate-temperature fuel cells and electrolyzers. *Adv. Mater.* **2006**, *18*, 1581–1584.
- (25) Ricote, S.; Bonanos, N.; Marco de Lucas, M. C.; Caboche, G. Structural and conductivity study of proton conductor $\text{BaCe}_{0.9-x}\text{Zr}_x\text{Y}_{0.1}\text{O}_{3-\delta}$ at intermediate temperatures. *J. Power Sources* **2009**, *193*, 189–193.
- (26) Słodczyk, A.; Sharp, M. D.; Upasen, S.; Colomban, P.; Kilner, J. A. Combined bulk and surface analysis of the $\text{BaCe}_{0.5}\text{Zr}_{0.3}\text{Y}_{0.16}\text{Zn}_{0.04}\text{O}_{3-\delta}$ (BCZYZ) ceramic proton-conducting electrolyte. *Solid State Ionics* **2014**, *262*, 870–874.
- (27) Tu, C.-S.; Chien, R. R.; Schmidt, V. H.; Lee, S. C.; Huang, C.-C. Temperature-dependent structure of proton conducting $\text{Ba}(\text{Zr}_{0.8-x}\text{Ce}_x\text{Y}_{0.2})\text{O}_{2.9}$ ceramics by Raman scattering and x-ray diffraction. *J. Phys.: Condens. Matter* **2012**, *24*, 155403.
- (28) Genet, F.; Lorient, S.; Ritter, C.; Lucazeau, G. Phase transitions in BaCeO_3 : neutron diffraction and Raman studies. *J. Phys. Chem. Solids* **1999**, *60*, 2009–2021.
- (29) Charrier-Cougoulic, I.; Pagnier, T.; Lucazeau, G. Raman Spectroscopy of perovskite-type $\text{BaCe}_x\text{Zr}_{1-x}\text{O}_3$ ($0 \leq x \leq 1$). *J. Solid State Chem.* **1999**, *142*, 220–227.
- (30) Artini, C.; Pani, M.; Lausi, A.; Masini, R.; Costa, G. A. High Temperature Structural Study of Gd-Doped Ceria by Synchrotron X-ray Diffraction ($673 \text{ K} \leq T \leq 1073 \text{ K}$). *Inorg. Chem.* **2014**, *53*, 10140–10149.
- (31) Artini, C.; Presto, S.; Massardo, S.; Pani, M.; Carnasciali, M. M.; Viviani, M. Transport Properties and High Temperature Raman Features of Heavily Gd-Doped Ceria. *Energies* **2019**, *12*, 4148.
- (32) Kreuer, K. D. Proton-Conducting Oxides. *Annu. Rev. Mater. Res.* **2003**, *33*, 333–359.
- (33) Kreuer, K. D. Aspects of the formation and mobility of protonic charge carriers and the stability of perovskite-type oxides. *Solid State Ionics* **1999**, *125*, 285–302.
- (34) Schmitt, R.; Nenning, A.; Kraynis, O.; Korobko, R.; Frenkel, A. I.; Lubomirsky, I.; Haile, S. M.; Rupp, J. L. M. A review of defect structure and chemistry in ceria and its solid solutions. *Chem. Soc. Rev.* **2020**, *49*, 554–592.
- (35) Trovarelli, A. Structural and oxygen storage/release properties of CeO_2 -based solid solutions. *Comments Inorg. Chem.* **1999**, *20*, 263–284.
- (36) Hudish, G.; Manerbino, A.; Coors, W. G.; Ricote, S. Chemical expansion in $\text{BaZr}_{0.9-x}\text{Ce}_x\text{Y}_{0.1}\text{O}_{3-\delta}$ ($x = \text{and } 0.2$) upon hydration determined by high-temperature X-ray diffraction. *J. Am. Ceram. Soc.* **2018**, *101*, 1298–1309.
- (37) Andersson, A. K. E.; Selbach, S. M.; Knee, C. S.; Grande, T. Chemical expansion due to hydration of proton-conducting perovskite oxide ceramics. *J. Am. Ceram. Soc.* **2014**, *97*, 2654–2661.
- (38) Mortalò, C.; Santoru, A.; Pistidda, C.; Rebollo, E.; Boaro, M.; Leonelli, C.; Fabrizio, M. Structural evolution of $\text{BaCe}_{0.65}\text{Zr}_{0.20}\text{Y}_{0.15}\text{O}_{3-\delta}$ – $\text{Ce}_{0.85}\text{Gd}_{0.15}\text{O}_{2-\delta}$ composite MPEC membrane by in-situ synchrotron XRD analyses. *Mater. Today Energy* **2019**, *13*, 331–341.
- (39) Larson, A. C.; Von Dreele, R. B. *General Structure Analysis System (GSAS)*; Los Alamos National Laboratory Report LAUR 86-748, 2000.
- (40) Toby, B. H. EXPGUI, a graphical user interface for GSAS. *J. Appl. Crystallogr.* **2001**, *34*, 210–213.
- (41) Pappacena, A.; Porreca, P.; Boaro, M.; de Leitenburg, C.; Trovarelli, A. Effect of process modification and presence of H_2O_2 in the synthesis of samaria-doped ceria powders for fuel cell applications. *Int. J. Hydrogen Energy* **2012**, *37*, 1698–1709.

- (42) Schmitt, R.; Nanning, A.; Kraynis, O.; Korobko, R.; Frenkel, A. I.; Lubomirsky, I.; Haile, S. M.; Rupp, J. L. M. A review of defect structure and chemistry in ceria and its solid solutions. *Chem. Soc. Rev.* **2020**, *49*, 554–592.
- (43) Luisetto, I.; Tuti, S.; Romano, C.; Boaro, M.; di Bartolomeo, E.; Kesavan, J. K.; Kumar, S. S.; Selvakumar, K. Dry reforming of methane over Ni supported on doped CeO₂: New insight on the role of dopants for CO₂ activation. *J. CO₂ Util.* **2019**, *30*, 63–78.
- (44) Slodczyk, A.; Zaafrani, O.; Sharp, M.; Kilner, J.; Dabrowski, B.; Lacroix, O.; Colomban, P. Testing the chemical/structural stability of proton conducting perovskite ceramic membranes by in situ/ex situ autoclave Raman microscopy. *Membranes* **2013**, *3*, 311–330.
- (45) Genet, F.; Loidant, S.; Lucazeau, G. Vibrational normal modes of the D_{2h}¹⁶ phase of BaCeO₃ a critical comparison of force fields. *J. Raman Spectrosc.* **1997**, *28*, 255–276.
- (46) Scherban, T.; Villeneuve, R.; Abello, L.; Lucazeau, G. Raman scattering study of acceptor-doped BaCeO₃. *Solid State Ionics* **1993**, *61*, 93–98.
- (47) Arrigoni, M.; Kotomin, E. A.; Maier, J. Large-scale modeling of defects in advanced oxides: Oxygen vacancies in BaZrO₃ crystals. In *High Performance Computing Science and Engineering*; Nagel, W. E., Kröner, D. H., Resch, M. M., Eds.; Springer: Cham, Switzerland, 2016; Vol. 15, pp 187–198.
- (48) Han, D.; Majima, M.; Uda, T. Structure analysis of BaCe_{0.8}Y_{0.2}O_{3-δ} in dry and wet atmospheres by high-temperature X-ray diffraction measurement. *J. Solid State Chem.* **2013**, *205*, 122–128.
- (49) Banerji, A.; Grover, V.; Sathe, V.; Deb, S. K.; Tyagi, A. K. CeO₂/Gd₂O₃ system: Unraveling of microscopic features by Raman spectroscopy. *Solid State Commun.* **2009**, *149*, 1689–1692.
- (50) Hernández, W. Y.; Laguna, O. H.; Centeno, M. A.; Odriozola, J. A. Structural and catalytic properties of lanthanide (La, Eu, Gd) doped ceria. *J. Solid State Chem.* **2011**, *184*, 3014–3020.
- (51) Xu, Y.; Wang, F.; Liu, X.; Liu, Y.; Luo, M.; Teng, B.; Fan, M.; Liu, X. Resolving a decade-long question of oxygen defects in Raman spectra of ceria-based catalysts at atomic level. *J. Phys. Chem. C* **2019**, *123*, 18889–18894.
- (52) Sartoretti, E.; Novara, C.; Giorgis, F.; Piumetti, M.; Bensaid, S.; Russo, N.; Fino, D. In situ Raman analyses of the soot oxidation reaction over nanostructured ceria based catalyst. *Sci. Rep.* **2019**, *9*, 3875. , and reference therein
- (53) Andriopoulou, C.; Trimpalis, A.; Petalidou, K. C.; Sgoura, A.; Efstathiou, A. M.; Boghosian, S. Structural and redox properties of Ce_{1-x}Zr_xO_{2-δ} and Ce_{0.8}Zr_{0.15}Re_{0.05}O_{2-δ} (RE:La, Nd, Pr, Y) solids studies by high temperature in situ Raman spectroscopy. *J. Phys. Chem. C* **2017**, *121*, 7931–7943.
- (54) Schilling, C.; Hofmann, A.; Hess, C.; Ganduglia-Pirovano, M. V. Raman spectra of polycrystalline CeO₂: A density functional theory study. *J. Phys. Chem. C* **2017**, *121*, 20834–20849.
- (55) McBride, J. R.; Hass, K. C.; Poindexter, B. D.; Weber, W. H. Raman and X-ray studies of Ce_{1-x}Re_xO_{2-y} where Re= La, Pr, Nd, Eu, Gd, and Tb. *J. Appl. Phys.* **1994**, *76*, 2435–2441.
- (56) Colomban, P.; Slodczyk, A. Raman intensity: An important tool to study the structure and phase transitions of amorphous/crystalline materials. *Opt. Mater.* **2009**, *31*, 1759–1763.
- (57) Guo, M.; Lu, J.; Bi, Q.; Luo, M. Effect of optical absorbance on Raman spectra of Ce_{0.9}Tb_{0.1}O_{2-δ} solid solution. *ChemPhysChem* **2010**, *11*, 1693–1699.
- (58) Maher, R. C.; Cohen, L. F.; Lohsoontorn, P.; Brett, D. J. L.; Brandon, N. P. Raman spectroscopy as a probe of temperature and oxidation state for gadolinium-doped ceria used in solid oxide fuel cells. *J. Phys. Chem. A* **2008**, *112*, 1497.
- (59) Li, L.; Chen, F.; Lu, J.-Q.; Luo, M.-F. Study of defect site in Ce_{1-x}M_xO_{2-δ} (x=0.2) solid solution using Raman spectroscopy. *J. Phys. Chem. A* **2011**, *115*, 7972–7977.
- (60) Lucazeau, G. Effect of pressure and temperature on Raman spectra of solids: anharmonicity. *J. Raman Spectrosc.* **2003**, *34*, 478–496.
- (61) Muhich, C. L. Re-evaluating CeO₂ expansion upon reduction: non counterpoised forces, not ionic radius effects, are cause. *J. Phys. Chem. C* **2017**, *121*, 8052–8059.
- (62) García-Melchor, M.; López, N. Homolytic products from heterolytic paths in H₂ dissociation on metal oxides: The example of CeO₂. *J. Phys. Chem. C* **2014**, *118*, 10921–10926.
- (63) Gao, Y.; Li, R.; Chen, S.; Luo, L.; Cao, T.; Huang, W. Morphology-dependent interplay of reduction behaviors, oxygen vacancies and hydroxyl reactivity of CeO₂ nanocrystals. *Phys. Chem. Chem. Phys.* **2015**, *17*, 31862–31871.